Journal of Quantitative Spectroscopy & Radiative Transfer 279 (2022) 108063

Contents lists available at ScienceDirect

Journal of Quantitative Spectroscopy & Radiative Transfer

journal homepage: www.elsevier.com/locate/jqsrt

O_2–O_2 CIA in the gas phase: Cross-section of weak bands, and continuum absorption between 297–500 nm

Henning Finkenzeller, Rainer Volkamer*

Department of Chemistry & CIRES, University of Colorado Boulder, 215 UCB, Boulder, 80309, CO, USA

ARTICLE INFO

Article history:
Received 2 October 2021
Revised 29 December 2021
Accepted 30 December 2021
Available online 4 January 2022

Keywords:
Absorption cross section
Oxygen
Collision-induced absorption
Heating rate
DOAS
Remote sensing

ABSTRACT

Oxygen–oxygen collision-induced absorption (O_2–O_2 CIA) of solar radiation heats the atmosphere, affects radiative transfer, and needs to be considered in spectroscopy applications in Earth's atmosphere. The lack of O_2–O_2 CIA spectra in the gas phase below 335 nm wavelength is limiting remote sensing applications in this spectral range. This study reports measurements of the O_2–O_2 CIA cross-section in the gas phase at high signal-to-noise ratio and spectral resolution, sufficient to fully resolve spectral band shapes (0.31–0.42 nm FWHM, full width at half maximum) using Cavity Enhanced Extinction Spectroscopy at atmospheric pressure, and variable temperature (293, 263, and 223 Kelvin). Excellent agreement with literature spectra is observed for selected strong bands. Several heretofore unmeasured weak absorption bands are characterized for the first time in the gas phase under controlled laboratory conditions, i.e., the bands centered at 315 and 328 nm ($b^1\Sigma_g^+ + b^1\Sigma_g^+ \leftarrow X^3\Sigma_g^- + X^3\Sigma_g^-$, vibrational quanta change $\Delta\nu_{tot} = 4, 3$), 420 nm ($a^1\Delta_g + b^1\Sigma_g^+ \leftarrow X^3\Sigma_g^- + X^3\Sigma_g^-, \Delta\nu_{tot} = 2$), and 495 nm ($a^1\Delta_g + a^1\Delta_g \leftarrow X^3\Sigma_g^- + X^3\Sigma_g^-, \Delta\nu_{tot} = 3$). The band shape at 344 nm deviates from the available literature, in part owing to the overlap of neighboring bands that give rise to non-zero continuum absorption. The consistency of spectral band shapes of transitions with non-zero $\Delta\nu_{tot}$ is used to predict the absorption bands at 301 nm ($b^1\Sigma_g^+ + b^1\Sigma_g^+ \leftarrow X^3\Sigma_g^- + X^3\Sigma_g^-$, $\Delta\nu_{tot} = 5$), and 397 nm ($a^1\Delta_g + b^1\Sigma_g^+ \leftarrow X^3\Sigma_g^- + X^3\Sigma_g^-, \Delta\nu_{tot} = 3$). A complete O_2–O_2 CIA cross section spectrum is presented between 297–500 nm, that is optimized for use in hyperspectral (and other) remote sensing applications.

1. Introduction

Collision-induced absorption (CIA) is the absorption in systems of interacting atoms or molecules, where the absorption exceeds the simple sum of the absorption by the isolated atoms and molecules [1–5]. For oxygen, electronic transitions forbidden for isolated molecules by both spin and electric dipole selection rules become possible in O_2–O_2 interactions. The absorption α_{CIA} [cm^{-1}] related to binary O_2–O_2 CIA scales with the square of the oxygen concentration c_{O_2} [6]:

$$\alpha_{CIA} = \sigma_{CIA} c_{O_2}^2 \quad (1)$$

Here, σ_{CIA} is the CIA cross section [$cm^5\,molec^{-2}$]. The combined change of electronic state and total vibrational quantum ν_{tot}, i.e. the net change of vibronic quanta of the participating $X^3\Sigma_g^-$, $b^1\Sigma_g^+$, and $a^1\Delta_g$ states of molecular oxygen during the transition, gives rise to series of transitions that extend across the UV to NIR spectral range (Fig. 1). Theory describes the structure of the observed absorption features in general terms, but is not yet able to predict the cross section at the level of accuracy and precision required in many spectroscopy applications. Specifically, neither the exact line shape nor the strength of different transitions can be predicted accurately.

The O_2–O_2 collision complex in the atmosphere is a natural greenhouse gas, and O_2–O_2 CIA is a source of singlet oxygen suggested to be relevant in atmospheric chemistry [8]. The total absorption of incoming solar radiation for mid-latitude overhead sun amounts to ~ 1.07 W m^{-2} in the visible range alone, and 2.03–2.31 W m^{-2} total [9].

O_2–O_2 CIA overlaps with the absorption of numerous trace gases of interest to atmospheric chemistry, and therefore needs to be accounted for in the retrieval of gases such as formaldehyde, glyoxal, nitrogen dioxide, nitrous acid, chlorine dioxide, bromine oxide radicals, iodine oxide radicals, sulfur dioxide and others [10,11] that are relevant to discussions about air quality and lifetimes of climate active gases such as ozone and methane. Fig. 2 shows the optical density of O_2–O_2 CIA ($\tau_{O_2O_2}$) for two geometries:

* Corresponding author.

https://doi.org/10.1016/j.jqsrt.2021.108063

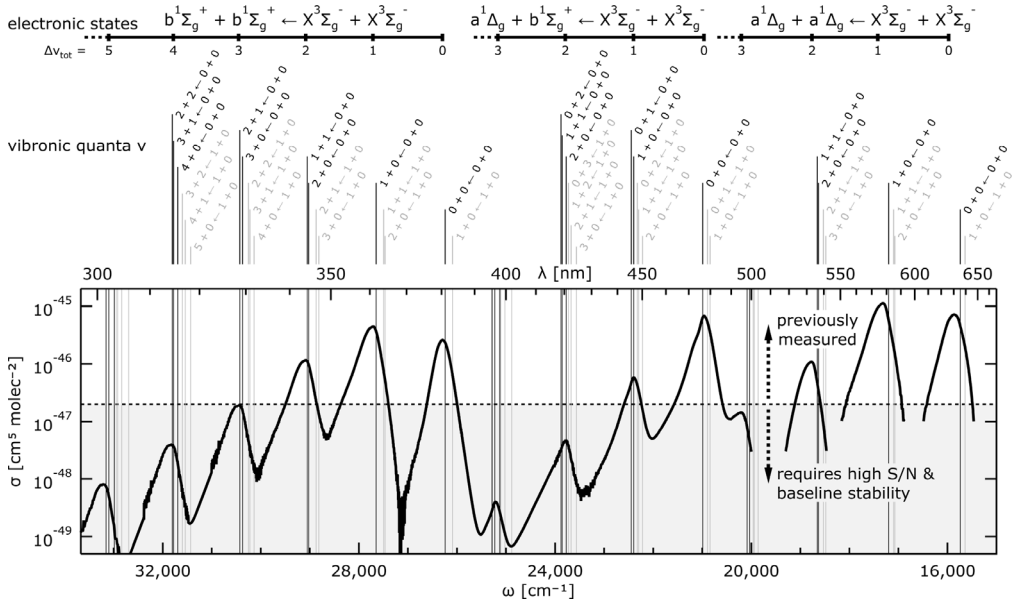

Fig. 1. σ_{CIA} (298 K) in the UV-Vis spectral range. Data for wavelengths larger 500 nm are adapted from Thalman and Volkamer [7]. Vibronic transitions involving ground states (black) and vibrationally excited oxygen (grey) give rise to overlapping spectral features that modify apparent band shapes, and give rise to non-zero broad band absorption not previously quantified.

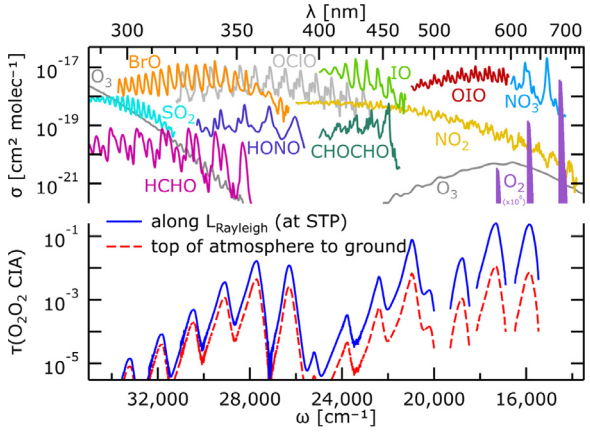

Fig. 2. Overlap between O_2–O_2 CIA and atmospheric trace gases at UV-Vis wavelengths. Also the weaker lines can reach strengths that are significant for the remote sensing of other gases.

Extinction along the Rayleigh scattering path at standard temperature and pressure (STP), and from the top of atmosphere to the ground. As can be seen, even weak lines can cause optical depths of $\sim 10^{-4}$, comparable to the optical depths caused by weakly absorbing trace gases. The incorrect representation of σ_{CIA} in the interpretation of spectra can cause interferences. In the UV spectral range, Pinardi et al. [12] explicitly studied the sensitivity of HCHO retrievals towards different literature σ_{CIA} and concluded that significant interferences occur between σ_{CIA}, HCHO, and BrO absorption features in the 336.5–359 nm interval. Extending the retrieval interval towards the UV, to include more absorption features of HCHO, has to some extent been limited by the lack of reference spectra for σ_{CIA} below 335 nm.

α_{CIA} in the atmosphere can be accurately predicted if the atmospheric temperature and humidity profile are known [7]. Therefore, oxygen is of interest as a calibration gas to determine air mass factors, and constrains radiative transfer simulations to characterize aerosols that influence the Earth radiation balance.

While good σ_{CIA} spectra are needed for the above reasons, laboratory measurements at atmospherically relevant conditions are challenging. For the most meaningful results, large columns have to be attained by using long light paths, and avoiding high oxygen pressures, which introduce pressure broadening and terneray interactions. The temperature dependence [e.g. 7,13] needs to be resolved, an effect that is particularly relevant for measurement geometries that cover a wide range of temperatures, i.e., all satellite geometries [14] and airborne measurements [11,15]. There is a long legacy of studies investigating σ_{CIA} in various experimental conditions. Numerous laboratory studies analyzed the absorption in the UV-Vis spectral ranges in the gas phase [6,7,16–31], in the liquid phase [32–37], and in solid oxygen [38]. Perner and Platt [39] included σ_{CIA} for the first time in the interpretation of atmospheric spectra, and σ_{CIA} has been determined from atmospheric observations in direct sun geometries [13,40,41].

Still, for the transitions at 420, 328, and 315 nm, spectrally resolved data in the gas phase currently do no exist. Lampel et al. [42] detected the bands at 328 and 420 nm in the atmosphere, highlighting the need for more complete absorption cross sections.

The more recent development of cavity enhanced extinction spectroscopy (CEES) has created the capability to create large gas columns in a compact instrument via long light paths, rather than high pressures. The compact design allows for a straight-forward temperature control, such that measurements can be carried out at close-to-atmospheric conditions. While the stronger absorption features of O_2–O_2 CIA have been characterized using this technique [7,31], the measurements of the weak bands have been impeded by (1) progressively stronger Rayleigh scattering at UV wavelengths, limiting the effective path length inside the optical cavity to few km only (confer Table 1), (2) small signals requiring a high level of precision, and (3) limited availability of suitable mirror-light source combinations.

Using CEES with optimized optical components, an automated data acquisition and analysis scheme, long integration times in a stabilized setup, and by using pure oxygen at atmospheric pressure, this study provides information on the heretofore unresolved absorption of the weak bands in the UV-Vis range below 500 nm, generating a cross section that is complete in regards to the needs

Table 1
Experimental Setup: Configuration and characterization.

Spectral range nm	Light source	Filter	mirror	σ_{CIA} band [nm]	Setup L^a_{Ar} [km]	Opt. density $D = \frac{I_{Ar}}{I_{O_2}} - 1$	FWHM [nm]
307–349	LDLS	WG320, UG11, dichroic	Layertec	315	0.60	$1.4 \cdot 10^{-4}$	0.31[b,f]
				328	1.1	$1.3 \cdot 10^{-3}$	
				344	1.0	$7.2 \cdot 10^{-3}$	
349–397	LDLS	CVI320, UG11	ATFilms	360	2.0	$5.6 \cdot 10^{-2}$	0.40[c,f]
				380	1.6	$2.6 \cdot 10^{-2}$	
408–427	LED[h]	SP450	CRD Optics	420	7.0	$2.0 \cdot 10^{-3}$	0.42[d,f]
427–498	LED[i]	GG430	ATFilms	447	16	$5.7 \cdot 10^{-2}$	0.35[e,g]
				477	12	$5.0 \cdot 10^{-1}$	
				495	1.0	$9.0 \cdot 10^{-4}$	

a: Photon path length in argon, b: Spectral resolution, expressed as the full width half maximum (FWHM) of atomic emission lines; Hg at 334 nm, c: Kr at 368 nm, d: Kr at 432 nm, e: Kr at 450 nm, f: grating with 2400 grooves mm^{-1}, g: grating with 1200 grooves mm^{-1}, h: Lumiled L1F3-U410200014000, i: LED Engin LZ1-10B201

in atmospheric spectroscopy. To cover the temperature range relevant for spectroscopic atmospheric sensing, the cross section was determined at three temperatures: +20 °C, for surface and laboratory applications, −10 °C, the typical effective temperature of the total column in direct sun measurements, and −50 °C, as found in the upper troposphere by satellite and aircraft.

2. Experiment and data analysis

The O_2–O_2 CIA cross section is determined from the measurement of spectral light extinction due to oxygen, i.e., the combination of O_2–O_2 CIA and oxygen Rayleigh scattering. The spectral path length in the optical cavities and the reference light fluxes are constrained from spectral flux measurements in the presence of argon and helium [43], i.e., two noble gases with distinct Rayleigh scattering cross sections that are well-described by theory due to the absence of a King correction factor [44]. The contribution of oxygen Rayleigh scattering to the total extinction is accounted for using theory.

2.1. Experimental setup

The experimental apparatus is shown in Fig. 3. It builds on a setup used by Thalman and Volkamer [7], but is optimized regarding stability and automation for long integration times, and employs optical elements and light sources optimized for the new spectral ranges. We used either LEDs or a laser driven light source (LDLS, Energetiq EQ99FX, purged with nitrogen, coupled by a 650 μm fiber) to provide measurement light in the desired spectral range. Filtering of out-of-band light – light that is not cavity-enhanced and interferes as stray light – is established with a short focal length collimating lens and different filters (Table 1). Mirrors are one inch in diameter with a radius of 1 m. Temperature control of the cavity jacket is the same as in Thalman and Volkamer [7]. The surrounding transfer optics are held at a constant temperature to minimize drifts. Using pure oxygen instead of air mixtures enhances the signal by a factor of approximately 25 without distorting the cross section or introducing ternary interactions [26]. Measurements are carried out at ambient pressure (Boulder, CO, ~ 800 hPa), which is monitored by electronic pressure transducers (Honeywell) and calibrated periodically by a mercury barometer. We used an Acton 2150 Czerny-Turner grating spectrometer (Princeton Instruments) and a PIXIS400B scientific camera (Princeton Instruments) to record spectra. A spectral resolution of 0.31–0.42 nm ensures full sampling of the bands.

To minimize measurement bias from lamp intensity drifts while allowing for long total integration time necessary for photon statistics, an automated recurring measurement sequence was developed. Every gas is sampled in periods of 7 min duration only,

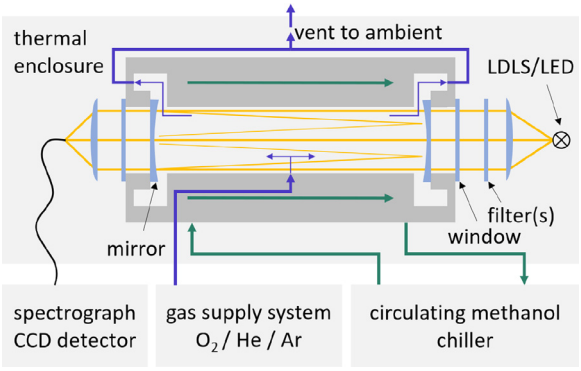

Fig. 3. Sketch of the experimental setup. Building on Thalman and Volkamer [7], the setup has improved stability, the optical bench and transfer optics (specifically, filters) are held at a constant temperature; gases are injected in the center of the cavity and vented symmetrically through a shared port.

shorter than the characteristic light source drift times of approximately 15 min. Transitions between gases are established with 3 min of high purge flow (1 lpm), while for the remaining 4 min the purge is reduced to 0.1 lpm, to minimize gas consumption and prevent back diffusion. Intensities of adjacent argon spectra (the closer half of the 4 min low flow spectrum) are averaged between adjacent sets, which in first order compensates for lamp drifts. Higher order lamp drift effects cancel out statistically. Following this procedure, ratios of oxygen, argon, and helium are co-added to reduce photon shot-noise. The intensity ratio I_{Ar}/I_{He}, informing the photon path length, is distinct from unity on the order of several percent and does therefore not need to be measured at the same level of absolute precision as measurements of I_{Ar}/I_{O_2}, where optical thicknesses can be as small as $1.4 \cdot 10^{-4}$. Accordingly, most of the measurement time is dedicated to characterize I_{Ar}/I_{O_2}. Only every fifth ratio of gases, recurring hourly, is dedicated towards characterizing I_{Ar}/I_{He}. This ratio is interpolated to the measurement time of the oxygen spectra. Pressure changes are not significant on this timescale. Pressure changes that occur over longer timescales are considered in the data analysis.

2.2. Data inversion to derive σ_{CIA}

The theoretical path length L_{vac} [cm] in an evacuated cavity without extinction from neither absorption nor scattering is given by:

$$L_{vac} = \frac{b}{1-R} = \frac{1 - \frac{I_{Ar}}{I_{He}}}{\frac{I_{Ar}}{I_{He}} c_{Ar} \sigma^{Ray}_{Ar} - c_{He} \sigma^{Ray}_{He}} \quad (2)$$

where b is the distance between the mirrors [cm], and R is the mirror reflectivity [unitless]. L_{vac} can be determined from comparing spectral fluxes I_x [cts bin^{-1} s^{-1}] in the presence of gases x, where c_x is the concentration [molec cm^{-3}] of gas x calculated from measurements of temperature and pressure, and σ_x^{Ray} is the Rayleigh scattering cross section [cm^2 molec^{-1}] taken from the literature [44–46]. In this study, argon and helium were used as gases with well-known σ_x^{Ray}. The effective optical thickness D describes the attenuation of light inside the cavity:

$$D = c_x \sigma_x L_{vac} = \frac{I_{vac}}{I_x} - 1 \tag{3}$$

where σ_x is the extinction cross section [cm^2 molec^{-1}] of gas x, and I_{vac} is the theoretical spectral flux in vacuum. Eq. (3) takes into account that any extinction process necessarily reduces the length a photon travels inside the optical resonator (self-limitation) [47]. Solving Eq. (3) for I_x leads to:

$$I_x = \frac{I_{vac}}{1 + c_x \sigma_x L_{vac}} \Leftrightarrow I_{vac} = I_x (1 + c_x \sigma_x L_{vac}) \tag{4}$$

For argon and oxygen, considering that σ_{O_2} has contributions from $\sigma_{O_2}^{Ray}$ and σ_{CIA}:

$$I_{vac} = I_{Ar} (1 + c_{Ar} \sigma_{Ar}^{Ray} L_{vac}) \tag{5}$$

$$= I_{O_2} (1 + c_{O_2} \sigma_{O_2}^{Ray} L_{vac} + c_{O_2}^2 \sigma_{CIA} L_{vac}) \tag{6}$$

where σ_{CIA} is the O_2–O_2 CIA cross section [cm^5 molec^{-2}]. Solving for σ_{CIA} and assuming no significant pressure and temperature changes between the measurement of I_x for different gases ($c_{Ar} = c_{He} = c_{O_2} = c$) yields:

$$\sigma_{CIA} = \frac{1}{c} \left[\underbrace{\left(\frac{I_{Ar}}{I_{O_2}} - 1 \right)}_{D} \underbrace{\left(\frac{\frac{I_{Ar}}{I_{He}} \sigma_{Ar}^{Ray} - \sigma_{He}^{Ray}}{1 - \frac{I_{Ar}}{I_{He}}} + \sigma_{Ar}^{Ray} \right)}_{\frac{1}{cL_{Ar}}} - \underbrace{\left(\sigma_{O_2}^{Ray} - \sigma_{Ar}^{Ray} \right)}_{\Delta_{\sigma^{Ray}}} \right] \tag{7}$$

where D is the optical thickness as defined in Eq. (3), L_{Ar} is the path length [cm] in argon, Δ_σ [cm^2 molec^{-1}] is the difference in Rayleigh scattering cross section between oxygen and argon. Notably, Eq. (7) does not explicitly involve instrument specific parameters such as b, R or L_{Ar}, but derives σ_{CIA} directly from knowledge of σ_x^{Ray} and the measured spectral fluxes.

2.3. Baseline correction

Even when great care is taken to minimize interferences and instabilities during the measurement process, data acquisition and analysis following Eq. (7) will initially yield a raw cross section σ_{CIA}^{raw} that is not free of artifacts, and a baseline B needs to be subtracted: $\sigma_{CIA} = \sigma_{CIA}^{raw} - B$. This baseline is not well understood and could have different origins, but can be constrained experimentally, as described below. As in the measurement process the extinction of oxygen, i.e., the combination of $\sigma_{O_2}^{Ray}$ and σ_{CIA}, is determined, σ_{CIA} needs to be isolated from $\sigma_{O_2}^{Ray}$ following Eq. (7). Incorrect descriptions of $\sigma_{O_2}^{Ray}$ and σ_{Ar}^{Ray} could bias $\Delta_{\sigma^{Ray}}$ and introduce a baseline. We also speculate that the slightly different refractive indeces of gases affect the coupling of measurement light into and out of the optical cavity [48]. In particular, the refraction of non-perpendicular light on surfaces of the transfer optics will differ slightly if the bath gas changes. The reflectivity across the mirror surfaces is not fully uniform, and slight differences in the instrument illumination for the different gases will influence the light path. Ultimately, the need to correct this baseline reflects an uncertainty in σ_{CIA}. This baseline is small and not limiting the overall accuracy for strong bands, but it can limit the overall uncertainty of the weaker bands (Table 2).

Table 2
Error budget. The measured uncertainty is estimated as the quadratic sum of all individual parameter uncertainties, including baseline correction; the final error leverages trend information for weak bands.

parameter	uncertainty [%]		
	individual	measured	final
temperature	< 1		
pressure	0.1		
fill purity	< 1		
σ_{Ar}^{Ray}	1		
baseline correction			
303 nm*			97*
315 nm	214	214	65*
328 nm	33	33	33
344 nm	7.3	7.7	7.7
360 nm	0.40	2.5	2.5
380 nm	0.46	2.5	2.5
397 nm*			16*
420 nm	40	40	40
447 nm	4.0	4.7	4.7
477 nm	0.3	2.5	2.5
495 nm	28	28	28

*: extrapolated based on trend information, see Sect. 2.4.

To constrain the baseline, we exploit that the wings of individual transitions fall off approximately exponentially in wavenumber space [1,29,49]. We assume the following shape for the baseline B in each spectral range covered in a measurement:

$$B(\omega) = c_0 + c_1\omega + c_2\omega^2 + c_3 \underbrace{\frac{\sigma_{Ar}^{Ray}(\omega) - \sigma_{He}^{Ray}(\omega)}{(1 - \frac{I_{Ar}}{I_{He}}(\omega))^2}}_{\partial\left(\frac{I_{Ar}}{I_{He}}\right)^{1/L_{Ar}}} + c_4 \underbrace{\frac{2(\sigma_{Ar}^{Ray}(\omega) - \sigma_{He}^{Ray}(\omega))}{(1 - \frac{I_{Ar}}{I_{He}}(\omega))^3}}_{\partial^2\left(\frac{I_{Ar}}{I_{He}}\right)^{1/L_{Ar}}} \tag{8}$$

where ω are wavenumbers [cm^{-1}], and c_i scaling coefficients. The last two terms are motivated by the assumption that the variation in coupling efficiency between helium and argon transfers to the coupling efficiency variation between argon and oxygen. To determine the coefficients c_i we exploit that for each notch $\vee_k$, i.e. the spectral ranges between transition centers, the true cross section can be approximated by the superposition of the red and blue wing (dashed lines in Fig. 4) of the adjacent transitions:

$$\sigma_{CIA}(\omega^{\vee_k}) \approx \sigma_{CIA}^{\vee_k}(\omega^{\vee_k}) = \underbrace{r_k \exp(R_k \omega^{\vee_k})}_{\text{red}} \text{ wing} + \underbrace{b_k \exp(-B_k \omega^{\vee_k})}_{\text{blue}} \text{ wing} \tag{9}$$

where $R_k, B_k > 0$ are the fitted slopes of the red and blue wing [cm], and $r_k, b_k > 0$ scaling factors [cm^5 molec^{-2}]. Then, for the entire set of $\omega^{\vee_k}$ covered in one measurement, we choose fit parameters that optimize $\sigma_{CIA}^{raw} - B - \sigma^{\vee} \to 0$. This fitting approach is robust for stronger bands. For weaker bands the slope of the corresponding wings from adjacent vibrational transitions with good signal-to-noise ratio (SNR) is adopted. The parameterization of the notches helps to merge data of adjacent wavelength ranges, acquired with a different setup configuration, with only minimal

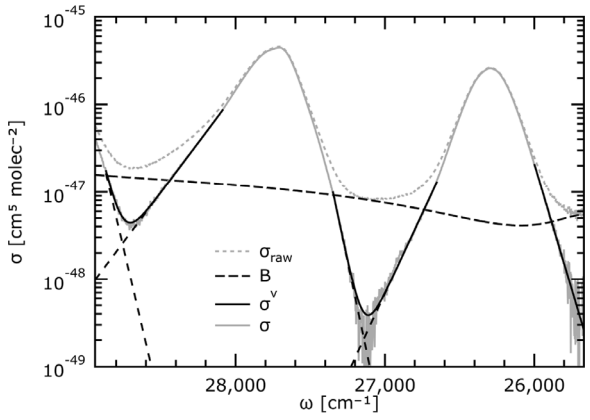

Fig. 4. Example of baseline correction. The baseline B is determined and subtracted from σ_{raw} such that the corrected $\sigma = \sigma_{raw} - B \approx \sigma^{\vee}$ in notches.

discontinuities and distortion. The baseline correction influences the retrieved shape of the transition in the far wings, but it only marginally influences the width of the transition and the line shape as a whole.

2.4. Predicting extremely weak transitions

The extremely weak transitions $b^1\Sigma_g^+ + b^1\Sigma_g^+ \leftarrow X^3\Sigma_g^- + X^3\Sigma_g^-$, $\Delta\nu_{tot} = 5$, and $a^1\Delta_g + b^1\Sigma_g^+ \leftarrow X^3\Sigma_g^- + X^3\Sigma_g^-$, $\Delta\nu_{tot} = 3$, (Fig. 1) have been detected previously [33,36], but were not measured directly in this study. In this study we leverage information from measurements with lower $\Delta\nu_{tot}$ to predict the absorption in these transitions, and to generate smoother data for the transition $b^1\Sigma_g^+ + b^1\Sigma_g^+ \leftarrow X^3\Sigma_g^- + X^3\Sigma_g^-$, $\Delta\nu_{tot} = 4$. Specifically, we exploit that band shape, position and line strength follow distinct trends [36] that justify extrapolation. In this study, we used peak absorption strength to predict the strength of missing transitions, but integral cross section could be used similarly. The trends are discussed in Sections 3.1 and 3.2.

2.5. Wavelength accuracy and error budget

Wavelength calibration is achieved by recording a spectrum of solar scattered light, and comparing the position of numerous Fraunhofer lines (present at all wavelengths) by spectral fitting of a literature solar spectrum [50]. The wavelength of the σ_{CIA} spectrum is reported as wavelength in vacuum, with an uncertainty of less than 0.01 nm.

The accuracy of the determined σ_{CIA} depends on the accuracy of the parameters in Eq. (7) and on the extent that the instrument properties vary for different gases. Temperature control is better than 1%, as in Thalman and Volkamer [7]. Ultra high purity Ar (99.998%), He (99.998%), O_2 (99.994%) was used. The completeness of gas exchanges was monitored via spectral intensity measurements and is better than 1%. The total concentration uncertainty is therefore better than 2%. Notably, Eq. (7) neither depends specifically on the mirror separation, nor on mirror reflectivity, but σ_{CIA} is derived directly from measured intensities. Eq. (3) is accurate even for the strongest absorption band studied (477 nm), where relative deviations of D from the exact solution are much smaller than 10^{-4} [47,51]. The uncertainty of σ_{Ar}^{Ray} was estimated to be $< 1\%$ [44,52]. For oxygen a King correction factor is needed, with an uncertainty of $< 1\%$ [46]. The uncertainty in $\sigma_{O_2}^{Ray}$ is therefore larger, but only contributes in decoupling the oxygen Rayleigh cross section from the collision induced absorption (Eq. (7)). It thus only introduces a baseline in σ_{CIA}^{raw}, but does not affect the scaling of the cross section. Uniform intensity shifts during sets of argon and oxygen measurements may add to the baseline, but do not affect the differential signal that ultimately determines σ_{CIA}. The uncertainty due to baseline correction (Section 2.3) was estimated as the standard deviation between baselines determined for the three temperatures at the wavenumber of peak absorption. The resulting total accuracy for the different transitions is estimated in Table 2 as quadratic sum of the individual uncertainty sources.

It is difficult to estimate the uncertainty for the extrapolated transitions. The observed trends for position and strength are clear, but not rigorously explained by theory. The differences predicted for different temperatures are not believed to be significant but rather representative for the accuracy of the measurements. Errors propagated from fits to the band position (linear spacing) and peak absorption (exponentially weakening with increasing $\Delta\nu_{tot}$), using uncertainties as weights, yield estimates for the uncertainty in the final data (Table 2). The transition at 315 nm was measured directly, but to avoid artifacts from relatively poor SNR in practical application, trend information and the band shape of the adjacent transition at 328 nm is leveraged for this transition.

3. Results & discussion

Analysis as outlined above yields cross sections as shown in Fig. 5.

3.1. Spectral band shapes

The O_2–O_2 CIA spectrum is the result of absorption in pairs of singlet oxygen molecules of different vibrational excitation (Fig. 1). Notably, for a given $\Delta\nu_{tot}$, the observed line shape is generally not due to a single pair of transitions, but results from combinations of multiple transitions. Fig. 6 shows the normalized absorption relative to the wavenumber of peak absorption for transitions with given $\Delta\nu_{tot}$ within the different electronic systems ($b^1\Sigma_g^+ + b^1\Sigma_g^+$, $b^1\Sigma_g^+ + a^1\Delta_g$, $a^1\Delta_g + a^1\Delta_g$) at $T = 293$ K. The latter data are adapted from Thalman and Volkamer [7] and given for reference. The line shape is not the same for the transitions in the different electronic systems, and there are also differences within the systems. Within the $b^1\Sigma_g^+ + b^1\Sigma_g^+ \leftarrow X^3\Sigma_g^- + X^3\Sigma_g^-$ band, the shape of the $\Delta\nu_{tot} = 0$ line is markedly different from transitions with higher $\Delta\nu_{tot}$. The former can be remarkably well approximated by a simple Voigt profile (dashed line in Fig. 6). While similar is also observed as a good approximation for the $\Delta\nu_{tot} = 0$ transition of the $a^1\Delta_g + a^1\Delta_g$ system, it does not apply to the $\Delta\nu_{tot} = 0$ transition of the $a^1\Delta_g + b^1\Sigma_g^+$ system. Within the latter system, the line shapes appear to all be rather consistent with each other. Possible explanations for the different band shape for $\Delta\nu_{tot} = 0$ transitions in the symmetrical systems are further discussed in Section 4.3.

The transition $a^1\Delta_g + b^1\Sigma_g^+ \leftarrow X^3\Sigma_g^- + X^3\Sigma_g^-$, $\Delta\nu_{tot} = 2$ was measured at relatively poor SNR, such that the deviation of the band shape from the $\Delta\nu_{tot} = 0, 1$ transitions is not believed to be significant.

3.2. Line positions and strength

Fig. 7 shows the position, peak absorption, width (FWHM), and integral cross section for measured and extrapolated transitions within the two electronic bands measured at $T = 293$ K. The hollow markers indicate extrapolated properties, crosses data used for extrapolation. Distinct trends are clearly visible, with the exception of the $b^1\Sigma_g^+ + b^1\Sigma_g^+ \leftarrow X^3\Sigma_g^- + X^3\Sigma_g^-$, $\Delta\nu_{tot} = 0$ transition, which is markedly different in that it exhibits a significantly narrower

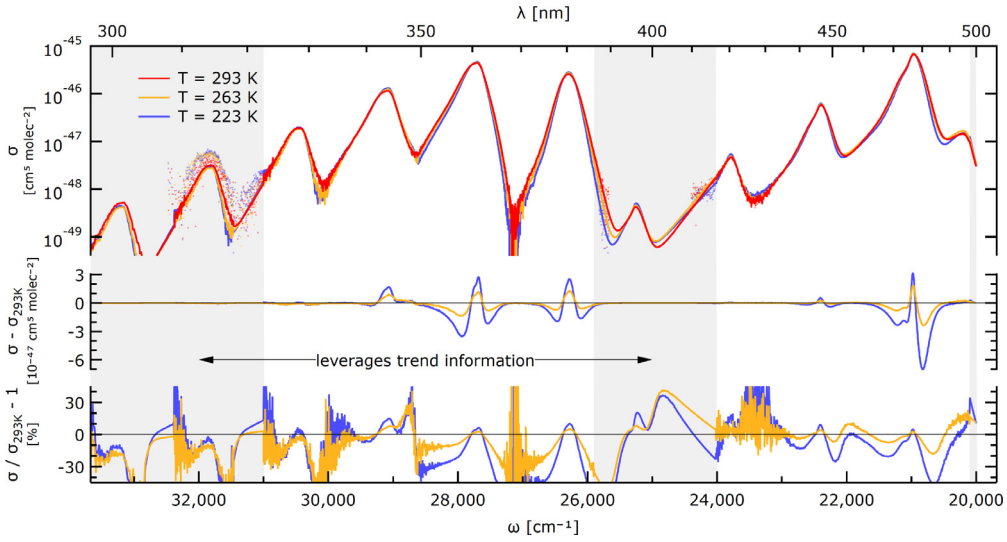

Fig. 5. The cross section at T =223, 263, and 293 K. Measurements (dotted) and complete composite cross section (lines). The middle panel shows absolute differences of the cold cross sections to the cross section at 293 K ($\Delta\sigma = \sigma_T - \sigma_{293\,K}$), the bottom panel shows the ratio ($\Delta\sigma = \sigma_T/\sigma_{293\,K} - 1$).

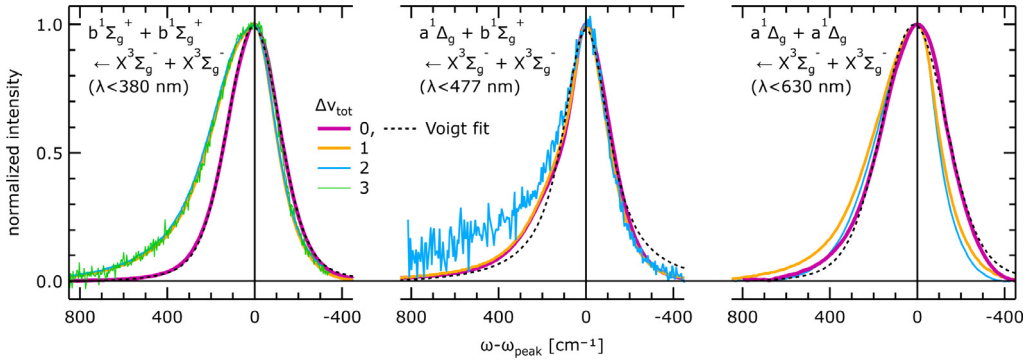

Fig. 6. Line shapes for the three electronic transitions in the UV-Vis spectral range for different $\Delta\nu_{tot}$ within each system. The asymmetry in line shape for transitions with $\Delta\nu_{tot} = 0$ in like pairs of oxygen molecules is less pronounced than in transitions that involve distinguishable molecules. Data for $a^1\Delta_g + a^1\Delta_g \leftarrow X^3\Sigma_g^- + X^3\Sigma_g^-$ are adapted from Thalman and Volkamer [7].

Table 3
Oscillator strengths [10^{-43} cm^4 molec^{-2}] and relative oscillator strengths for the electronic transitions below 477 nm. Bracketed values indicate hypothetical oscillator strengths under the assumption of a zero-baseline between transitions in this study.

	Greenblatt et al. [24]	Hermans et al. [26]	Thalman and Volkamer [7]	This study (no baseline)	
	$b^1\Sigma_g^+ + b^1\Sigma_g^+ \leftarrow X^3\Sigma_g^- + X^3\Sigma_g^-$, $\lambda < 380$ nm				
abs.	3.51	2.66	2.82	3.18	(3.08)
rel.	1.10	0.83	0.88	1	(0.97)
	$a^1\Delta_g + b^1\Sigma_g^+ \leftarrow X^3\Sigma_g^- + X^3\Sigma_g^-$, $\lambda < 477$ nm				
abs.	2.16	2.13	2.16	2.41	(2.24)
rel.	0.90	0.88	0.90	1	(0.93)

FWHM (compare Section 3.1), more than an order of magnitude smaller peak absorption and integral cross section compared to the extrapolated values.

3.3. Oscillator strength

The oscillator strength for the two measured electronic transitions is given in Table 3. The effect of baseline correction methods on the oscillator strength is illustrated by bracketed values that indicate hypothetical oscillator strengths calculated under the assumption of a zero-baseline correction, i.e., the assumption that CIA assumes zero between transitions. This analysis suggests that the baseline contributes approximately 7% in the blue spectral range and 3% in the UV spectral range. A complete table of integral cross sections for different $\Delta\nu_{tot}$ is given in Table S2.

3.4. Comparison of gas-phase measurements in the laboratory

Fig. 8 compares the σ_{CIA} spectrum at $T = 293$ K with available literature cross sections in the UV-Vis spectral range. The more recent cross section determined in He et al. [31] was recorded at relatively poor SNR, limiting the ability for a meaningful comparison. For clarity it is omitted in the middle and bottom panel of Fig. 8; it seems to be consistently smaller in the UV spectral range, especially at 360 nm. For the other cross sections shown, there is generally good agreement, and differences are generally understood in terms of differences in the methods used for baseline correction, and SNR.

Evidently, the exponentially decreasing absorption in the line wings leads to overlap between neighboring transitions that gives rise to a broad band continuum absorption that spans much of the

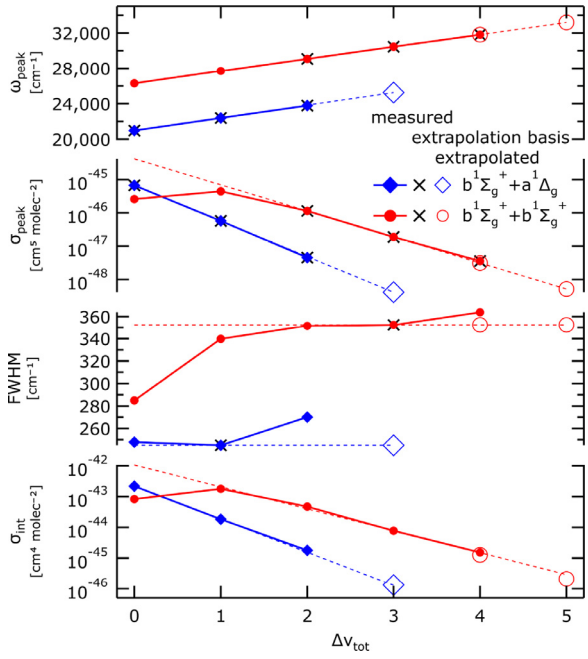

Fig. 7. Trend analysis of line properties as a function of $\Delta\nu_{tot}$ at T = 293 K: ${}^1\Sigma_g^+ + {}^1\Sigma_g^+$ (UV) and ${}^1\Sigma_g^+ + {}^1\Delta_g$ (blue). Bold markers indicate measured quantities, crosses indicate quantities used for extrapolation, hollow markers indicate extrapolated quantities.

UV-Vis spectral range as shown in Fig. 8. This significant baseline absorption between the transitions is on the order of few percent of the adjacent peak cross section values. Hermans et al. [26] and Thalman and Volkamer [7] made the assumption that σ_{CIA} is zero in the minima between neighboring O_2–O_2 bands (see Fig. 8); those ranges were used as supporting points to approximate their baseline with a polynomial. Greenblatt et al. [24] did not make a zero-baseline assumption, but the low SNR in the measurements, and high pressures applied in that study did not allow to accurately constrain and resolve the baseline absorption minima.

No direct comparison is possible at 315, 328, 420, 495 nm, as this study is the first to resolve these transitions. This is due to limited SNR and limited spectral coverage. For the strong transitions at 477, 360, and 380 nm, the agreement is good, with deviations of few to several percent (for peak cross section values compare Table S2). The larger cross section found in this study is partially explained by the contribution of the underlying baseline. For the 344 nm transition, the determined absorption is notably wider and stronger than in Hermans et al. [26] and Thalman and Volkamer [7], likely because of a limited spectral range and the zero-baseline assumption in these studies. For the 447 nm transition, σ_{CIA} in Hermans et al. [26] and Thalman and Volkamer [7] is approximately 10% smaller than in this study, and Greenblatt et al. [24] reports a significant baseline. For the 495 nm transition, no spectrally resolved data exist for direct comparison. However, the absorption position and strength is consistent with the trends in the $a^1\Delta_g + a^1\Delta_g \leftarrow X^3\Sigma_g^- + X^3\Sigma_g^-$ system (Fig. 1).

For a comparison of the differential cross sections, σ'_{CIA}, as it is typically used in DOAS fitting, see Section 4.1 and Table 4.

3.5. Comparison of weak transitions with liquid phase measurements

For the weak bands, where no previous laboratory measurements in the gas phase are available, a semi-quantitative comparison is possible with measurements in liquid O_2 by Dianov-Klokov [36]. The interaction of oxygen molecules in the liquid-phase (at $T = 78$ K [36]) is distinct from interactions in relatively dilute gases (at $T = 293$ K), but still meaningful [19], and is also supported from the comparisons shown in Table S1. Absorption strengths are compared relative to the $\Delta\nu_{tot} = 1$ transition, and the measured cross sections are found to be in reasonable agreement for peak wavelength and peak absorption. Specifically, for the weak transitions at 315 and 328 nm the relative absorption strength and the position agree within uncertainties with the data of Dianov-Klokov [36]. While the position for the extremely weak 301 and 397 nm transitions is given in Dianov-Klokov [36], the absorption strength is not unambiguously apparent in the publication and could therefore not be compared. The transition at 397 nm is predicted at the essentially the same position, for the 301 nm transition the position predicted in this study is 1.9 nm shorter than reported in Dianov-Klokov [36]. Direct measurements would be needed to assess whether this difference is at least partially also the result of our extrapolation method. The transition at 495 nm agrees reasonably well with Dianov-Klokov [36] both in position and magnitude, while the transition at 420 nm agrees well in the position, but the lower absorption strength is only marginally compatible with

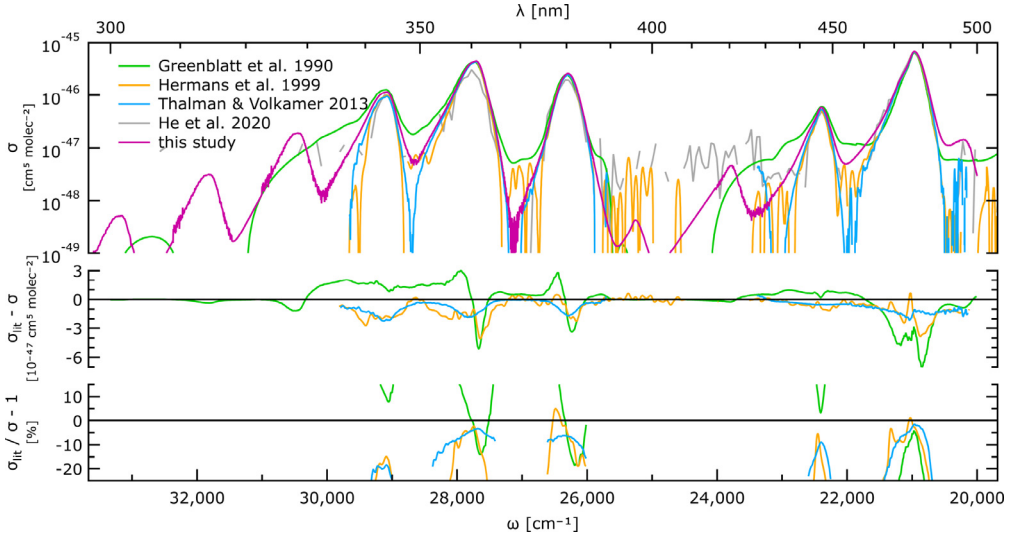

Fig. 8. Comparison with literature spectra. The middle panel shows the absolute difference of this study's cross section to the literature ($\Delta\sigma = \sigma_{lit} - \sigma$), whereas the bottom panel shows the relative difference ($\Delta\sigma = \sigma_{lit}/\sigma - 1$, data were filtered for $\sigma \geq 2.5 \cdot 10^{-47}$ cm^5 molec^{-2}) for clarity.

Table 4
DOAS fit comparison of the differential σ_{CIA} with the literature. c is the fit factor ($\sigma_{CIA} - c \cdot \sigma_{CIA,lit} \rightarrow 0$), and RMS is the fit residual (root mean square) as indicator of systematic differences in spectral features.

Target gas	Retrieval interval	Polyn. degree	Greenblatt et al. [24]		Hermans et al. [26]		Thalman and Volkamer [7]	
	[nm]		c^a	RMS^b	c^a	RMS^b	c^a	RMS^b
HCHO, BrO	336.5–359	5	1.010	$7.4 \cdot 10^{-5}$	0.956	$1.3 \cdot 10^{-4}$	1.102	$3.8 \cdot 10^{-5}$
NO_2, O_2–O_2	338–370	5	1.082	$4.4 \cdot 10^{-4}$	0.987	$2.2 \cdot 10^{-4}$	1.032	$7.9 \cdot 10^{-5}$
NO_2, O_2–O_2	425–490	5	1.008	$2.8 \cdot 10^{-4}$	0.994	$2.1 \cdot 10^{-4}$	1.000	$6.0 \cdot 10^{-5}$

a: fit uncertainty negligible; b: assuming an O_2–O_2 CIA slant column of $4 \cdot 10^{43}$ molec^2 cm^{-5}

the liquid-phase measurement. The comparison of spectral band shapes is not possible due to the lack of reference spectra in digital format for liquid oxygen.

3.6. Comparison of weak transitions with field measurements

Lampel et al. [42] estimated the transition position and relative peak absorption from regression analysis in atmospheric field data, by transferring the band shape of the 344 nm transition to approximately 328 nm and of the 447 nm transition to approximately 420 nm. Then, the exact position was derived from allowing the absorption feature to shift, the relative strength was derived from fitting the column and comparing it to the column fitted for transitions at 344 and 447 nm. Table S1 compares our laboratory measurements with the estimates made in Lampel et al. [42]. The transition at 328 nm is in good agreement regarding both peak position and absorption strength, but quantified with lower error bars. The transition at 420 nm is in good agreement regarding peak absorption. The transition position is notably longer than in Lampel et al. [42]. The reason for the relatively large uncertainties in Lampel et al. [42] for this transition lies in the absorption of water vapor as poorly constrained interference in this spectral range in atmospheric spectra.

3.7. Temperature dependence

Fig. 5 shows the cross section for $T = +20, -10, -50\,^{\circ}C$. It is clearly discernible in the strong transitions how the peak cross section increases towards lower temperatures and how the band width decreases, consistent with previous studies and the idea that the interaction time scales with the thermal velocity [1]. For the very weak transitions with large $\Delta\nu_{tot}$ measurements have a lower relative accuracy and give no strong indication whether for all $\Delta\nu_{tot}$ peak cross sections at cold temperature are generally stronger than at warm temperature. The comparison of the cross section at different temperatures yields an interesting feature: The transition $a^1\Delta_g + a^1\Delta_g \leftarrow X^3\Sigma_g^- + X^3\Sigma_g^-$, $\Delta\nu_{tot} = 4$, is discernible at 473 nm, overlaid by the strong transition $a^1\Delta_g + b^1\Sigma_g^+ \leftarrow X^3\Sigma_g^- + X^3\Sigma_g^-$, $\Delta\nu_{tot} = 0$ (middle and bottom panel in Fig. 5). The absorption added by this transition is $< 1\%$, but might be relevant for rigorous interpretations of the band shape.

Fig. 9 shows the peak absorption and integral absorption of selected bands as scalars in comparison with literature data. The 360 and 477 nm transition are chosen for comparison as they offer goodSNR, the 380 nm transition was chosen as it stands out within the UV transitions in regard to band shape and intensity (Section 4.3). The peak absorption cross section increases with decreasing temperature, consistent with Thalman and Volkamer [7], but seemingly varies less strongly with temperature as in that study. Related, the new baseline method affects the integral cross section, which consistently shows a marginally significant decrease with temperature. Hollow circles indicate hypothetical cross sections if a zero-baseline was assumed in this study, as used in Hermans et al. [26] and Thalman and Volkamer [7]. They illustrate the contribution of the temperature dependent baseline. For the transition at 380 nm a baseline is virtually absent. The slight decrease of the integral cross section towards colder temperatures seems to be marginally significant, and is worthy of further study. Oscillator strengths increasing with temperature have been found repeatedly for other systems. With increasing temperature closer encounters occur, which leads to stronger induced dipole moments and thus greater intensities [1].

4. Implications & outlook

4.1. Implications for DOAS retrievals

Differential Optical Absorption Spectroscopy (DOAS) [10,53] is a technique widely used to retrieve certain trace gases in the UV-Vis spectral ranges (Fig. 2). It builds on the idea that distinct narrow-band absorption features of trace gases can be separated from broad-band effects that influence the spectral fluxes smoothly, e.g. Rayleigh or Mie scattering and molecular continuum absorption. In DOAS fits, observed optical densities are reconstructed by linearly combining cross sections of trace gases, differential with respect to a polynomial in the wavelength retrieval interval, and a polynomial.

Table 4 shows what scaling factors c are needed in the framework of a DOAS retrieval for literature σ_{CIA} to maximize closure to σ_{CIA} determined in this study. For the typical 425–490 nm retrieval window, scaling factors are essentially 1 for all cross sections. Deviations increase toward shorter wavelengths, where this study adds new information. The magnitude of retrieved O_2–O_2 CIA columns is the critical parameter informing radiative transfer calculations to determine air mass factors and cloud top heights. The magnitude of σ_{CIA} directly affect closure studies of O_2–O_2 CIA in the atmosphere, which currently give mixed results [54,55].

RMS (root-mean-square of the DOAS fit residual) is an indicator for what systematic structures arise in the optical density from fitting σ_{CIA} that have slightly different spectral features. Table 4 lists RMS assuming a typical O_2–O_2 slant column of $4 \cdot 10^{43}$ molec^2 cm^{-5}. RMS is found to be generally below $5 \cdot 10^{-4}$ (unitless residual optical density). For comparison, optical densities of weak atmospheric absorbers can be on the order of $\sim 10^{-4}$. RMS is consistently lowest ($< 8 \cdot 10^{-5}$) for comparison to Thalman and Volkamer [7]. It needs to be noted that the performed test is only indicative of the relative likeness between the different spectra, and does not replace thorough testing with the full complexity of real environments and retrievals. It is expected that a more accurate representation of O_2–O_2 CIA helps to reduce cross talk between difficult-to-retrieve absorbers like BrO and HCHO that are retrieved in the same retrieval interval, as illustrated in the abstract figure.

4.2. Implications for heating rates

The total absorption of incoming solar radiation due to O_2–O_2 CIA in the visible range alone is approximately 1 W m^{-2} [9], and uncertainties in σ_{CIA}, including continuum contributions, need to

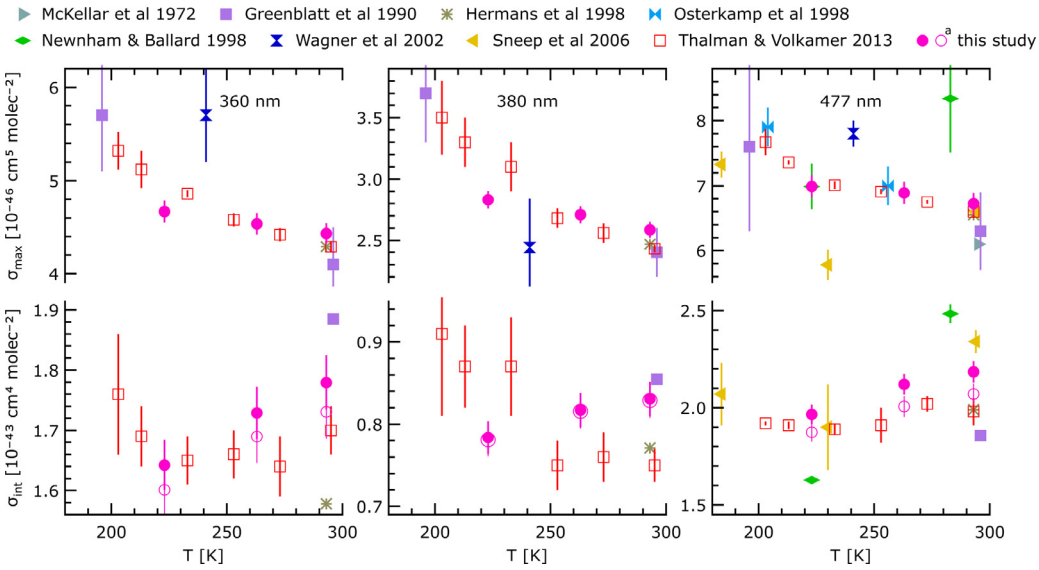

Fig. 9. Temperature dependence of the peak absorption and integral absorption at 360, 380, and 477 nm. Solid circles indicate data from this study, and hollow circles indicate the effect if the same data are reanalyzed assuming a zero-baseline.

be interpreted in this context. Table 3 shows the oscillator strength determined in this study in context with literature data. For the $a^1\Delta_g + b^1\Sigma_g^+ \leftarrow X^3\Sigma_g^- + X^3\Sigma_g^-$ band in the blue wavelength range differences reach up to 12%. Differences in the $b^1\Sigma_g^+ + b^1\Sigma_g^+ \leftarrow X^3\Sigma_g^- + X^3\Sigma_g^-$ band in the UV are even larger. Notably, the oscillator strength of the band in the red–green wavelength range is approximately 4 times larger than in the blue wavelength range ($\sim 8 \cdot 10^{-43}$ cm^4 molec^{-2}, Table S2). Considering the spectral distribution of solar incoming energy fluxes that decreases towards the UV spectral ranges, partially counteracted by stronger scattering at shorter wavelengths, the discrepancies found for σ_{CIA} in the UV and blue spectral range could account for errors in heating rates of several 0.01 W m^{-2}. Full radiative transfer calculations are needed to accurately assess the heating rates.

The continuum absorption as baseline for transitions contributes a few percent to the oscillator strength (Table 3) and must not be disregarded in calculations of heating rates. Greenblatt et al. [24] did not make the assumption of a zero baseline, but the SNR did not allow to resolve σ_{CIA} below $\sim 10^{-47}$ cm^5 molec^2, and data are influenced by the high oxygen pressures used. The cross section determined in this study differs from existing data in that it is the only to be spectrally complete in the 297–500 nm spectral range, it measured σ_{CIA} at atmospheric pressure and atmospheric temperatures, and it contains a physically motivated baseline. Thus, we believe that it is a good cross section to represent O_2–O_2 CIA in the atmosphere in this wavelength range. The effect of continuum absorption on the oscillator strengths of the red–green bands warrants to be checked.

4.3. Opportunity to develop theory

The extended range of vibronic quanta included in the measurements of O_2–O_2 CIA in the gas phase is an opportunity to test and develop theory. One should not disregard that observed line shapes generally result from the combination of multiple transitions with different rotational quanta in the incoming and outgoing molecules (Fig. 1). E.g., at room temperature, approximately 1 in 200 oxygen molecules is in its first vibrationally excited state. Consequently, observed trends might not be due to a single effect. The width of lines (FWHM ~ 300 cm^{-1} at $T = 293$ K, Fig. 9), has been contextualized with the duration of the collision, i.e. the radiatively active lifetime [1]. The width is also comparable to the kinetic energy change of the molecule pair involved (thermal energy at $T = 293$ K is equivalent to 204 cm^{-1}). The largest decrease in kinetic energy (red wings of lines) occurs when the relative velocity of the colliding molecules is reduced to essentially zero in a collision-induced absorption event. Increases in kinetic energy (blue wings) are not exceeding thermal energies considerably as result of the relatively weak interaction during the collision [19]. Effectively, the total line broadening due to change of kinetic energy can reach few 100 cm^{-1} (FWHM), comparable to lifetime broadening.

The different probabilities for kinetic energy gain and loss are understood to be the cause of the marked asymmetry of the lines and referred to as detailed balance or detailed equilibrium [1]. Detailed balance favors kinetic energy uptake, thereby introducing a blue shift: σ_{CIA} peak absorption positions are shifted blue relative to predictions that disregard kinetic energy changes, but only consider the energies of the involved oxygen molecules in different electronic and vibronic configuration (Fig. 1).

The asymmetry expected from detailed balance is not apparent in the transition $b^1\Sigma_g^+ + b^1\Sigma_g^+ \leftarrow X^3\Sigma_g^- + X^3\Sigma_g^-$, $\Delta\nu_{tot} = 0$ – and $a^1\Delta_g + a^1\Delta_g \leftarrow X^3\Sigma_g^- + X^3\Sigma_g^-$, $\Delta\nu_{tot} = 0$ – which can rather be approximated by a conventional symmetric Voigt profile (see Fig. 6, and Section 3.1). Additional to the band shape, the strength and width of this transitions does not follow the trend within the system (Fig. 9); specifically, the FWHM is 20% smaller than the other transitions, peak and integral absorption strengths are smaller than trend expectations by a factor 16 and 12, respectively. We hypothesize that these striking differences are due to the symmetry in the encounters, where pairs of indistinguishable molecules enter and leave the interaction. For collisions with weak coupling and negligible translational energy exchange, one would expect the line width to be dominated by lifetime broadening and to be essentially symmetric. The weak absorption (compared to $\Delta\nu_{tot} = 1$) suggest that these transitions are suppressed by a quantum selection criterion.

To our knowledge, the observed trend and the outlier from the trend in vibronic quanta has not previously been noted in the literature. The data of this study present an opportunity to further develop theory in the field of collision-induced electronic spectra.

4.4. Outlook

The extinction of light due to oxygen in the UV-Vis spectral ranges is not limited to O_2–O_2 CIA but includes Rayleigh extinction and molecular absorption. The contribution of these effects need to be considered correctly in experiments characterizing the optical properties of oxygen. The Rayleigh scattering cross section of oxygen $\sigma_{O_2}^{Ray}$ is constrained in the UV-Vis spectral range to only within 1%. Previous studies investigating $\sigma_{O_2}^{Ray}$ have assumed O_2–O_2 CIA to be absent in the 390–420 nm wavelength range and found larger positive deviations to theory at wavelengths between adjacent O_2–O_2 CIA transitions (340, 440, 460, and 520 nm [44]), consistent with non-zero CIA. The new σ_{CIA} spectra can be used to correct for the contribution of CIA, and to identify wavelengths that minimize – if not entirely avoid – O_2–O_2 CIA contribution in measurements of $\sigma_{O_2}^{Ray}$ at UV and visible wavelengths.

In the red spectral range CIA and molecular absorption of oxygen are overlaid (e.g., $a^1\Delta_g \leftarrow X^3\Sigma_g^-$, 630 nm, Fig. 2). Studies have used high spectral resolution and variations in pressure (molecular absorption scales linearly with pressure, binary CIA scales quadratically) to separate molecular absorption and CIA, but uncertainties remain in this spectral range. Cavity enhanced (broadband) extinction measurements have the potential to improve the characterization of O_2–O_2 CIA in this spectral range. Future studies should make an attempt at constraining the continuum absorption here, also because of its relevance to heating rates.

Cavity enhanced techniques can realize large columns via long light paths, rather than via high pressures, are compact and useful to allow good temperature control, and benefit from a spectral multiplexing advantage to measure entire bands simultaneously. Well defined optical paths are key for accurate cavity enhanced measurements. The measurement sequence used in this study achieves high SNR, but accuracy is not refined by this approach, and uncertainties remain. Setups that measure a very wide spectral range simultaneously can leverage information across the spectral range and thereby have the potential to better attribute signal variations to optical properties of oxygen (Rayleigh scattering, CIA, molecular absorption, potentially collision-induced scattering) and instrument effects. Cavity enhanced measurements that cover a very wide wavelength range with a single set of mirrors have so far provided only a moderate SNR and limited accuracy [31]. Prism-based optical resonators [56] have the potential to systematically exploit the multiplex advantages of cavity enhanced techniques, but also still face challenges.

5. Conclusions

The development of a stable high-finesse optical cavity, an optimized data acquisition procedure, and a physically motivated baseline correction allowed broadband measurements of O_2–O_2 CIA at high SNR at atmospherically relevant conditions. The generated data contribute to a more complete picture of O_2–O_2 CIA absorption in the gas phase. A cross section spectrum is generated for T= 223, 263, and 293 K that is complete in the 297–500 nm range. It includes previously unmeasured transitions and estimates for extremely weak transitions in this spectral range. It can be used in the interpretation of atmospheric spectra acquired in remote sensing applications of trace-gases and cloud top heights.

Where previous data exist, the measurements are shown to be in agreement with literature data in the gas phase, liquid phase, and inferences from atmospheric data. The differential cross sections are evaluated in fits using Differential Optical Absorption Spectroscopy, and found to agree well with literature cross sections for strong bands in the blue wavelength range. Deviations in the UV spectral range are attributed to the previously uncharacterized, and non-zero continuum absorption. The resolved band shapes are expected to more accurately account for O_2–O_2 CIA as interference in retrievals of other trace gases. While some benefits may exist at all wavelengths studied, the largest benefits are expected below 344 nm, and the new cross section is expected to help with the retrieval of trace gases like HCHO, BrO, HONO, etc., in the UV spectral range.

Differences in the integral cross section to literature data are approximately 10% in both the blue and UV spectral range, comparable to an atmospheric heating rate of few 0.01 W m^{-2}. The continuum absorption contributes 7% in the blue wavelength and 3% in the UV wavelength range. Knowledge about the non-zero O_2–O_2 CIA in the entire UV-Vis spectral range is valuable to guide future experiments constraining the Rayleigh scattering of oxygen that rely on the extinction of oxygen. This study confirms previous reports [7] that the peak cross section increases and the width of transition decreases at colder temperatures. However, a marginally significant increase of the integral cross section with temperature is observed, in line with the idea that higher temperatures lead to closer encounters, stronger induced dipoles and stronger absorption. More studies are required to reduce uncertainties in the temperature sensitivity. The generated data include a large range of vibronic quanta and are an opportunity to test and develop theory. Specifically, the questions that warrant to be addressed concern a deeper understanding of the factors that determine the integral absorption and line shape of individual transitions, and their relative distribution within a system. The transitions with indistinguishable pairs of molecules involved (e.g., $b^1\Sigma_g^+ + b^1\Sigma_g^+ \leftarrow X^3\Sigma_g^- + X^3\Sigma_g^-$, $\Delta\nu_{tot} = 0$) exhibit a strikingly symmetric line shape, different from expectations for CIA.

Data availability

Three O_2–O_2 CIA cross section files (223, 263, 293 K) are available for download as supplementary information to this publication, and from the following website: https://volkamergroup.colorado.edu/publications.

Funding

This work was supported by a NASA graduate fellowship NASA-NNX16AP36H, and NSF awards AGS-1620530, AGS-2027252.

Declaration of Competing Interest

The authors declare that they have no known competing financial interests or personal relationships that could have appeared to influence the work reported in this paper.

CRediT authorship contribution statement

Henning Finkenzeller: Methodology, Investigation, Formal analysis, Writing – original draft. **Rainer Volkamer:** Supervision, Resources, Writing – review & editing.

Acknowledgements

We would like to thank Tijs Karman, Iouli Gordon, Andrei Vigasin for stimulating ideas and discussions, and Theodore K. Koenig for comments on the manuscript.

Supplementary material

Supplementary material associated with this article can be found, in the online version, at doi:10.1016/j.jqsrt.2021.108063.

References

[1] Frommhold L. Collision-induced absorption in gases. cambridge ed. Cambridge: Cambridge University Press; 2006. ISBN 978-0-521-39345-4

[2] Camy-Peyret C, Vigasin AA. Weakly interacting molecular Pairs: unconventional absorbers of radiation in the atmosphere. Nato Science Series: IV:. Netherlands: Springer; 2012. ISBN 9789401000253, https://books.google.ch/books?id=GbwpBgAAQBAJ

[3] Slanina Z., Vigasin A.A.. Molecular complexes in Earth's, planetary, cometary, and interstellar atmospheres. 1998. doi:10.1142/3544

[4] Abel M, Frommhold L. Collision-induced spectra and current astronomical research. Can J Phys 2013;91(11):857–69. doi:10.1139/cjp-2012-0532.

[5] Karman T, Koenis MAJ, Banerjee A, Parker DH, Gordon IE, van der Avoird A, et al. O_2–O_2 and O_2–N_2 collision-induced absorption mechanisms unravelled. Nat Chem 2018;10(5):549–54. doi:10.1038/s41557-018-0015-x.

[6] Janssen J. Sur les spectres d'absorption de l'oxygène. Comptes rendus Hebd des seances l'Académie des Sci 1886;102:1352–3.

[7] Thalman R, Volkamer R. Temperature dependent absorption cross-sections of O_2–O_2 collision pairs between 340 and 630 nm and at atmospherically relevant pressure. Phys Chem Chem Phys 2013;15:15371–81. doi:10.1039/c3cp50968k. http://www.ncbi.nlm.nih.gov/pubmed/23928555

[8] Schurath U. Metastable oxygen molecules in the troposphere. Free Radic Res Commun 1987;3(1–5):173–84. doi:10.3109/10715768709069782.

[9] Solomon S, Portmann RW, Sanders RW, Daniel JS. Absorption of solar radiation by water vapor, oxygen, and related collision pairs in the Earth's atmosphere. J Geophys Res Atmos 1998;103(D4):3847–58. doi:10.1029/97JD03285.

[10] Platt U, Stutz J. Differential optical absorption spectroscopy; principles and applications. Physics of Earth and Space environments. Berlin Heidelberg: Springer-Verlag; 2008.

[11] Volkamer R, Baidar S, Campos TL, Coburn SC, DiGangi JP, Dix B, et al. Aircraft measurements of BrO, IO, glyoxal, NO_2, H_2O, O_2–O_2 and aerosol extinction profiles in the tropics: comparison with aircraft-/ship-based in situ and lidar measurements. Atmos Meas Tech 2015;8(5):2121–48. doi:10.5194/amt-8-2121-2015.

[12] Pinardi G, Van Roozendael M, Abuhassan N, Adams C, Cede A, Clémer K, et al. MAX-DOAS formaldehyde slant column measurements during CINDI: intercomparison and analysis improvement. Atmos Meas Tech 2013;6(1):167–85. doi:10.5194/amt-6-167-2013.

[13] Spinei E, Cede A, Herman J, Mount GH, Eloranta EW, Morley B, et al. Ground-based direct-sun DOAS and airborne MAX-DOAS measurements of the collision-induced oxygen complex, o_2o_2, absorption with significant pressure and temperature differences. Atmos Meas Tech 2015;8(2):793–809. doi:10.5194/amt-8-793-2015.

[14] Park SS, Takemura T, Kim J. Effect of temperature-dependent cross sections on O_4 slant column density estimation by a space-borne UVvisible hyperspectral sensor. Atmos Environ 2017;152:98–110. doi:10.1016/j.atmosenv.2016.12.020.

[15] Pfeilsticker K, Erle F, Platt U. Absorption of solar radiation by atmospheric O_4. J Atmos Sci 1997;54(7):933–9. doi:10.1175/1520-0469(1997)054<0933:AOSRBA>2.0.CO;2.

[16] Janssen J. Analyse spectrale des elements de l'atmosphère terrestre. Comptes rendus Hebd des seances l'Académie des Sci 1885;101:649–51.

[17] Janssen J. Sur les spectres de l'oxygène. Comptes rendus Hebd des seances l'Académie des Sci 1888;106:1118–19.

[18] Janssen J. Sur l'origine tellurique des raies de l'oxygène dans le spectre solaire. Comptes rendus Hebd des seances l'Académie des Sci 1889;108:1035–7.

[19] Salow H, Steiner W. Die durch wechselwirkungskräfte bedingten absorptionsspektra des sauerstoffes. Zeitschrift für Phys 1936;99(1):137–58. doi:10.1007/BF01847820.

[20] Robin J, Robin S. Spectre d'absorption visible et ultraviolet de l'oxygène comprimé jusqu'à 1 500 atmosphères. J Phys Radium 1954;15(4):331–4. doi:10.1051/jphysrad:01954001504033100.

[21] Tabisz GC, Allin EJ, Welsh HL. Interpretation of the visible and near-infrared absorption spectra of compressed oxygen as collision-induced electronic transitions. Can J Phys 1969;47(24):2859–71. doi:10.1139/p69-349.

[22] Blickensderfer RP, Ewing GE. Collision-induced absorption spectrum of gaseous oxygen at low temperatures and pressures. II. J Chem Phys 1969;51(12):5284–9. doi:10.1063/1.1671946.

[23] Blickensderfer RP, Ewing GE. Collisioninduced absorption spectrum of gaseous oxygen at low temperatures and pressures. I. J Chem Phys 1969;51(3):873–83. doi:10.1063/1.1672151.

[24] Greenblatt GD, Orlando JJ, Burkholder JB, Ravishankara AR. Absorption measurements of oxygen between 330 and 1140 nm. J Geophys Res Atmos 1990;95(D11):18577–82. doi:10.1029/JD095iD11p18577.

[25] McKellar ARW, Rich NH, Welsh HL. Collision-induced vibrational and electronic spectra of gaseous oxygen at low temperatures. Can J Phys 1972;50(1):1–9. doi:10.1139/p72-001.

[26] Hermans C, Vandaele AC, Carleer M, Fally S, Colin R, Jenouvrier A, et al. Absorption cross-sections of atmospheric constituents: NO_2, O_2, and H_2O. Environ Sci Pollut Res 1999;6(3):151–8. doi:10.1007/BF02987620.

[27] Newnham DA, Ballard J. Visible absorption cross sections and integrated absorption intensities of molecular oxygen (O_2 and O_4). J Geophys Res Atmos 1998;103(D22):28801–15. doi:10.1029/98JD02799.

[28] Naus H, Ubachs W. Visible absorption bands of the $(O_2)_2$ collision complex at pressures below 760 Torr. Appl Opt 1999;38(15):3423–8. doi:10.1364/AO.38.003423.

[29] Tiedje HF, DeMille S, MacArthur L, Brooks RL. Cavity ring-down spectroscopy of transient O_2–O_2 dimers. Can J Phys 2001;79(4):773–81. doi:10.1139/cjp-79-4-773.

[30] Sneep M, Ityaksov D, Aben I, Linnartz H, Ubachs W. Temperature-dependent cross sections of – collision-induced absorption resonances at 477 and 577 nm. J Quant Spectrosc Radiat Transf 2006;98(3):405–24. https://doi.org/10.1016/j.jqsrt.2005.06.004.

[31] He Q, Fang Z, Shoshamin O, Brown SS, Rudich Y. Scattering and absorption cross-sections of atmospheric gases in the ultraviolet-visible wavelength range (307–725 nm). Atmos Chem Phys Discuss 2020;2020(November):1–32.

[32] Ellis EW, Kneser HO. Kombinationsbeziehungen im absorptionsspektrum des flüssigen sauerstoffs. Zeitschrift für Phys 1933;86:583–91.

[33] Herman L. Spectre d'absorption de l'oxygène. Ann Phys 1939;11(11):548–611. doi:10.1051/anphys/193911110548.

[34] Dianov-Klokov VI. On the question of the origin of the spectrum of liquid and compressed oxygen (12600–3000 Å). Opt Spectrosc 1959;6(4):290–293.

[35] Dianov-Klokov VI. Absorption spectrum of oxygen at pressures from 2 to 35 atm in the region from 12600 to 3600 Å. Opt Spectrosc 1963:224–7.

[36] Dianov-Klokov VI. Absorption spectrum of condensed oxygen in the 1.26–0.3 μm region. Opt Spectrosc 1964:530–4.

[37] Dianov-Klokov VI. Absorption by gaseous oxygen and its mixtures with nitrogen in the 2800–2350 Å range. Opt Spectrosc 1965:233–6.

[38] Landau A, Allin EJ, Welsh HL. The absorption spectrum of solid oxygen in the wavelength region from 12,000 Å to 3300 Å. Spectrochim Acta 1962;18(1):1–19. doi:10.1016/0371-1951(62)80047-2.

[39] Perner D, Platt U. Absorption of light in the atmosphere by collision pairs of oxygen $(O_2)_2$. Geophys Res Lett - Geophys RES LETT 1980;7:1053–6. doi:10.1029/GL007i012p01053.

[40] Wagner T, von Friedeburg C, Wenig M, Otten C, Platt U. UV-visible observations of atmospheric O_4 absorptions using direct moonlight and zenith-scattered sunlight for clear-sky and cloudy sky conditions. J Geophys Res Atmos, AAC 3–1–AAC 3–15 2002;107(D20). doi:10.1029/2001JD001026.

[41] Osterkamp H, Ferlemann F, Harder H, Perner D, Platt U, Schneider M, et al. First measurement of the atmospheric O_4 profile. In: Harris NRP, Kilbane-Dawe I, Amanatidis GT, editors. Proceedings 4th European symposium on polar stratospheric ozone 1997. Schliersee, Germany: European Commision, Luxembourg; 1997. p. 478–81. http://hdl.handle.net/11858/00-001M-0000-0014-9848-6

[42] Lampel J, Zielcke J, Schmitt S, Pöhler D, Frieß U, Platt U, et al. Detection of O_4 absorption around 328 and 419 nm in measured atmospheric absorption spectra. Atmos Chem Phys 2018;18(3):1671–83. doi:10.5194/acp-18-1671-2018.

[43] Washenfelder RA, Langford AO, Fuchs H, Brown SS. Measurement of glyoxal using an incoherent broadband cavity enhanced absorption spectrometer. Atmos Chem Phys Discuss 2008;8(4):16517–53. doi:10.5194/acpd-8-16517-2008.

[44] Thalman R, Zarzana KJ, Tolbert MA, Volkamer R. Rayleigh scattering cross-section measurements of nitrogen, argon, oxygen and air. J Quant Spectrosc Radiat Transf 2014;147:171–7. doi:10.1016/j.jqsrt.2014.05.030.

[45] Peck ER, Fisher DJ. Dispersion of argon. J Opt Soc Am 1964;54(11):1362–4. doi:10.1364/JOSA.54.001362.

[46] Bates DR. Rayleigh scattering by air. Planet Space Sci 1984;32(6):785–90. doi:10.1016/0032-0633(84)90102-8.

[47] Platt U, Meinen J, Pöhler D, Leisner T. Broadband cavity enhanced differential optical absorption spectroscopy (CE-DOAS) – applicability and corrections. Atmos Meas Tech 2009;2(2):713–23. doi:10.5194/amt-2-713-2009.

[48] Fiedler SE, Hese A, Heitmann U. Influence of the cavity parameters on the output intensity in incoherent broadband cavity-enhanced absorption spectroscopy. Rev Sci Instrum 2007;78(7):73104. doi:10.1063/1.2752608.

[49] Borysow J, Moraldi M, Frommhold L. The collision induced spectroscopies concerning the desymmetrization of classical line shape. Mol Phys 1985;56(4):913–22. doi:10.1080/00268978500102801.

[50] Chance K, Kurucz RL. An improved high-resolution solar reference spectrum for Earth's atmosphere measurements in the ultraviolet, visible, and near infrared. J Quant Spectrosc Radiat Transf 2010;111(9):1289–95. doi:10.1016/j.jqsrt.2010.01.036.

[51] Horbanski M. A compact resonator based instrument for DOAS measurements of ambient nitrogen dioxide. University of Heidelberg; 2010. Diploma thesis.

[52] Sneep M, Ubachs W. Direct measurement of the Rayleigh scattering cross section in various gases. J Quant Spectrosc Radiat Transf 2005;92(3):293–310. doi:10.1016/j.jqsrt.2004.07.025.

[53] Platt U, Perner D. Measurements of atmospheric trace gases by long path differential UV/visible absorption spectroscopy BT - optical and laser remote sensing. In: Killinger DK, Mooradian A, editors. Optical and laser remote sensing. Berlin, Heidelberg: Springer Berlin Heidelberg; 1983. p. 97–105. doi:10.1007/978-3-540-39552-2_13. ISBN 978-3-540-39552-2

[54] Ortega I, Berg LK, Ferrare RA, Hair JW, Hostetler CA, Volkamer R. Elevated aerosol layers modify the O_2–O_2 absorption measured by ground-based MAX-DOAS. J Quant Spectrosc Radiat Transf 2016;176:34–49. https://doi.org/10.1016/j.jqsrt.2016.02.021.

[55] Wagner T, Beirle S, Benavent N, Bösch T, Chan KL, Donner S, et al. Is a scaling factor required to obtain closure between measured and modelled atmospheric O_4 absorptions? an assessment of uncertainties of measurements and radiative transfer simulations for 2 selected days during the MAD-CAT campaign. Atmos Meas Tech 2019;12(5):2745–817. doi:10.5194/amt-12-2745-2019.

[56] Johnston PS, Lehmann KK. Cavity enhanced absorption spectroscopy using a broadband prism cavity and a supercontinuum source. Opt Express 2008;16(19):15013–23 171927 [pii].